WILEY-VCH

Tailoring Anchoring Groups in Low-Dimensional Organic Semiconductor-Incorporated Perovskites

*Aihui Liang, Ke Ma, Yao Gao, and Letian Dou**

A. Liang
College of Chemistry and Chemical Engineering, Jiangxi Normal University, Nanchang 330022, China

A. Liang, K. Ma, Y. Gao, L. Dou
Davidson School of Chemical Engineering, Purdue University, West Lafayette, Indiana 47907, United States
E-mail: dou10@purdue.edu

L. Dou
Birck Nanotechnology Center, Purdue University, West Lafayette, Indiana 47907, United States

Keywords: (organic-inorganic hybrid perovskites, solar cells, passivation engineering, organic semiconductor-incorporated perovskites)

Abstract: Low dimensional, organic semiconductor-incorporated perovskites (OSiPs) are hybrid structures with functional organic cations intercalated between inorganic octahedron frameworks. They exhibit increased structural and compositional tunability, fascinating electronic properties, and enhanced stability for a wide range of applications. Currently, the interactions between the conjugated organic building blocks and the metal halide inorganic building blocks have not been fully investigated. Here, we report a series of bithiophene-based conjugated ligands with formamidinium, imidazolium and benzimidazolium terminal groups to examine the influence of different anchoring groups on the crystal structures, phase formation, and device performances. We showed that the terminal groups of the ligands have significant effect on the interactions between ligands and octahedra in perovskites, thus determine the formation of the crystal structures. While only the 3D perovskite solar cells passivated by the ligands with imidazolium and benzimidazolium terminal groups exhibit enhancement in power conversion efficiencies as well as reduced hysteresis. This report provides a new strategy of designing novel OSiPs structures and functionalities via tailoring the anchoring group.

1. Introduction

Metal halide perovskites are intensively researched in solar cells,[1] detectors,[2] field-effect transistors[3] and light emitting diodes,[4] owing to their outstanding properties, such as low-cost solution processability,[5] high absorption coefficient,[6] long charge carrier diffusion length,[7] high defect tolerance,[8] and narrow full width at half-maximum (FWHM) with high quantum yield.[9] Perovskite materials were first used for photovoltaic applications in 2009. Currently, the reported record efficiency for perovskite solar cells (PSCs) is over 25%.[10] Nevertheless, numerous crystal defects, including anion vacancies and uncoordinated lead cations, formed during fabrication, mostly at the surface and grain boundaries of the perovskite layer, and impair the stability and performance of PSCs. These defects remain as a significant hurdle for PSCs on the road to commercialization.[11] To address these issues, various methods are taken to enhance the overall stability of 3D perovskites, such as composition engineering,[12] interfacial modification,[13] passivation treatment,[14] and encapsulating procedures.[15] Apart from these strategies, another promising approach is to develop low-dimensional perovskites (2D, 1D and 0D), which exhibit enhanced stability and more structural and compositional versatility comparing with the 3D perovskites.[2d, 16]

There is a large number of functional organic molecules which show potential of being incorporated into 2D layered hybrid perovskites, including insulating aliphatic ammonium cations with large energy band gaps and poor charge transport properties, and semiconducting organic moieties such as aromatic pyrene, acene, diacetylene and carbazole units, which can further tune the electronic and optical properties of 2D perovskites.[17] In this regard, oligothiophene derivatives with tunable energy levels have recently received a lot of attentions.[3d, 5c, 18] Gao et al. synthesized several oligothiophene derivatives, including bithiophene (2T), tetrathiophene (4T) and methyl substitute tetrathiophene (4Tm) ammonium, as organic ligands for 2D organic-inorganic hybrid perovskites. The electronic structure and optical properties of 2D perovskites can be largely modulated through organic ligands, and highly stable perovskites were also achieved.[5c] Dunlap-Shohl et al. developed divalent oligothiophene-derived cations (AE_nT) by introducing protonated aminoethyl groups to both end of the oligothiophenes, which were successfully used in 2D perovskites.[18a] They showed that 2D perovskites incorporating conjugated organic cations enable unusual charge carrier interactions between organic and inorganic structural components. We have recently named this class of materials as organic semiconductor-incorporated perovskites (OSiPs).[19]

Although, a variety of conjugated moieties have been synthesized and incorporated into OSiPs, the anchoring groups used so far are mostly based on primary ammonium.[4b, 20]

As the $FAPbI_3$-based solar cells recently showed most promising results in reaching to Shockley-Queisser limit, the interactions between formamidinium (FA) and $[PbI_6]^{4-}$ octahedra becomes more interesting. In addition, imidazole (Im) and benzimidazole (BIm) have also been reported to have interactions with perovskite lattice and form low-dimensional perovskite or improve the crystallization.[21] In this manuscript, a series of bithiophene (2T)-based organic molecules with FA, Im and BIm terminal groups were synthesized to examine the effects of different anchoring groups on the formation of low-dimensional OSiPs, and the potential application in reducing electronic defects on perovskite surfaces. We showed that perovskite solar cells with interface tailored by these ligands exhibit different device performance. The efficiency increased from 19.59% for the control device, to 21.13% for the BIm ligand-passivated device. The improvement in device efficiency, especially the increase in open-circuit voltage (V_{OC}), is directly correlated with the low-dimensional crystal structure achieved with these ligands. These results provide a new direction in designing the organic molecules with different anchoring groups, and open a potential strategy in tuning the interactions between inorganic layer and the organic layer in low-dimensional perovskites.

2. Results and Discussion

The 2T-based organic cations with different terminal groups were firstly synthesized. After ligand synthesis, bulky crystals and thin films are prepared with these ligands to investigate the interactions between the anchoring groups and the $[PbI_6]^{4-}$ octahedral frameworks.

2.1. Synthesis

The synthetic routes of 2TFAI, 2TImI and 2TBImI ligands are shown in **Scheme 1**. In short, 2-(thiophen-2-yl)acetonitrile was reacted with N-bromosuccinimide to achieve compound **1**. Then compound **1** was coupled with tributyl(thiophen-2-yl)stannane through the palladium-catalyzed Stille coupling reaction to produce compound **2** in high yield. The compound **2** was reacted with sodium methoxide in methanol followed by the treatment with acetic acid and ammonium chloride, and then treated with aqueous hydrogen iodide to produce the target molecule 2TFAI. Compounds **4**, **5** and **6** were synthesized according to the literature methods. Compound **7** and **8** were synthesized from compound **5** and **6** respectively, reacted with compound **4** through Stille coupling reactions using $Pd_2(dba)_3$ as a catalyst and P(*o*-tolyl)$_3$ as a ligand. The desired molecules 2TImI and 2TBImI were obtained by the deprotection

reactions of compound **7** and **8** in the present of aqueous hydrogen iodide, respectively. All the chemical structures of the resulting organic ligands were confirmed by ^{1}H and ^{13}C nuclear magnetic resonance (NMR) spectroscopy and mass spectrometry (MS).

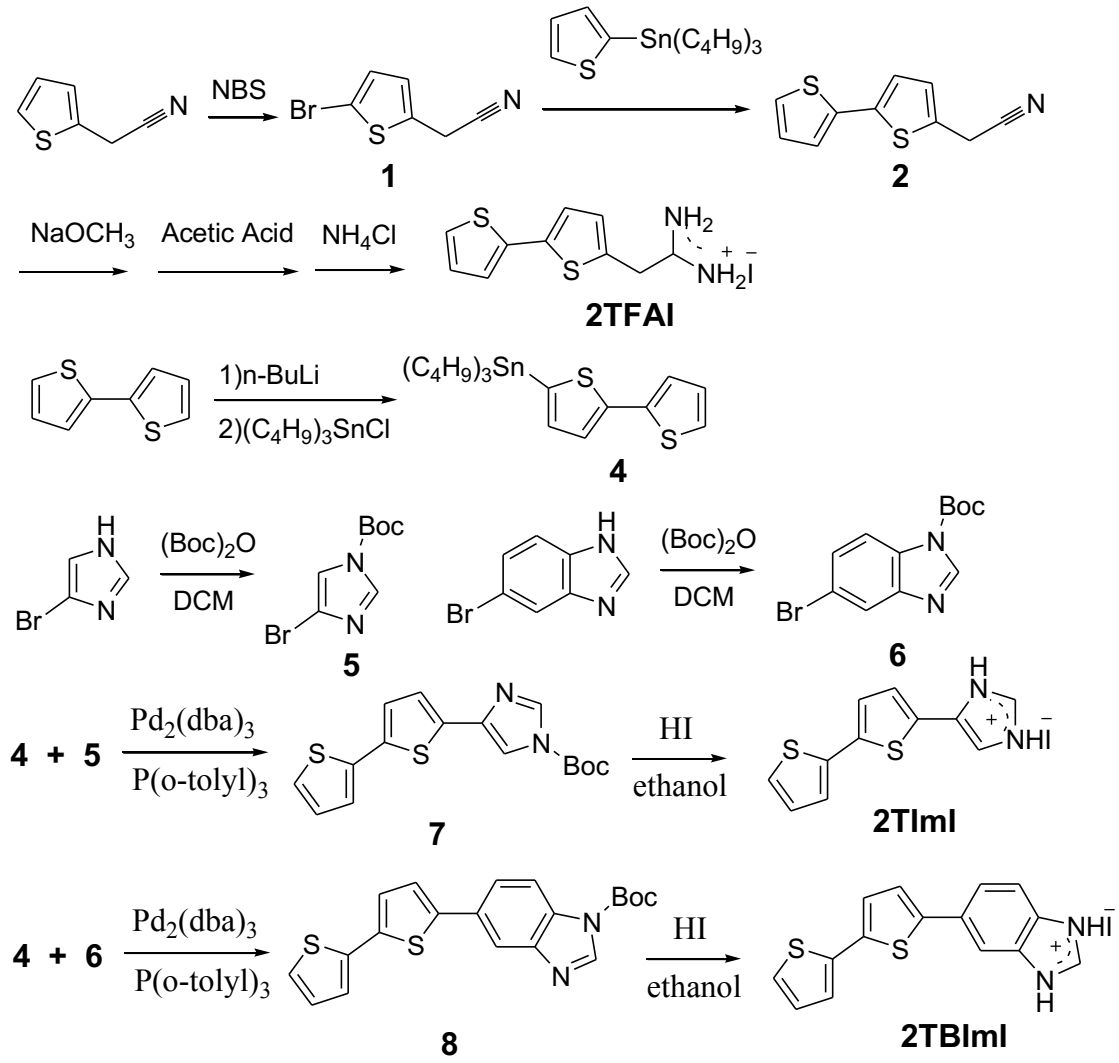

Scheme 1. The synthetic routes of ligands 2TFAI, 2TImI and 2TBImI.

2.2. Phase formation and degradation

In order to fabricate low-dimensional OSiP thin films with these conjugated ligands, precursor solutions with a stoichiometry of A_2BI_4 (with A being the conjugated ligands, B being either Pb or Sn) were prepared. Temperature-controlled absorption spectrum (T-UV) and X-ray diffraction spectrum (T-XRD) were carried out to analyze the formation and degradation of the thin films.

T-UV of $(2TIm)_2PbI_4$ was carried out on thin film that was dried at 70 ^{o}C for 10 min immediately after spin coating. A phase with a weak excitonic peak (at ~525 nm) presents (phase 1).[17a, 22] Then, as the temperature increases to 90 ^{o}C, a much more intense, but slightly

shifted excitonic peak appears at ~540 nm (phase 2, 2D), which is the characteristic of 2D layered lead iodide perovskite.[17d] Further increasing the temperature to ~110 °C causes the 2D perovskite peak to be weaker, while a new phase with an excitonic peak at ~460 nm (phase 3, 1D) starts to form. The phase 3 is expected to be a phase of an inorganic framework with a lower dimensionality, based on the significant shift of the excitonic peak to higher energy (**Figure 1**).[17a, 22] As the temperature increases to 150 °C, the peak at ~540 nm disappears, which indicates that the whole system is transformed to phase 3. T-XRD results are consistent with the T-UV results (**Figure S1**). At 70 °C, a weak crystalline phase with low dimensionality presents (phase 1). At 90 °C, a relatively higher dimensional crystalline phase is formed (phase 2), with an interplanar spacing of 18.87 Å. These results indicate that a 2D perovskite phase is formed, however the films are weakly crystallized. After the temperature increases to 130 °C, a new peak at about 5.27° appears which reflects phase 3, corresponding to the excitonic peak at ~460 nm in T-UV. $(2TBIm)_2PbI_4$ thin film exhibits similar T-UV and T-XRD behaviors as $(2TIm)_2PbI_4$ thin film (**Figure 1B and Figure S1**).

$(2TFA)_2PbI_4$ thin film exhibits different T-UV behavior with $(2TIm)_2PbI_4$ thin film (**Figure 1C**). When the thin film is dried at 70 °C for 10 min, a weak excitonic peak at ~456 nm appears (phase 2, 2D), which is correlated with the 2D layered lead iodide perovskite. While the temperature increases to 90 °C, this peak becomes stronger. At ~110 °C, this absorption peak weakens and another excitonic peak at ~430 nm shows up (phase 3, 1D). While further increasing the temperature to 150 °C, the peak at ~456 nm disappears, which indicates that phase 2 is completely transformed to phase 3. However, there is only one weak crystalline phase (phase 2, at ~5.2°) in T-XRD when the annealing temperature increases from 70 °C to 130 °C. No peak of 1D crystalline phase (phase 3) is observed (**Figure S1**).

In addition to the Pb-based thin films, we've also fabricated the Sn-based films to further investigate the interactions between ligands and $[SnI_6]^{4-}$ octahedra. **Figure 1D-F** and **Figure S2** shows the formation and degradation of $(2TIm)_2SnI_4$, $(2TBIm)_2SnI_4$ and $(2TFA)_2SnI_4$ thin films. $(2TIm)_2SnI_4$ and $(2TBIm)_2SnI_4$ show similar T-UV and T-XRD behaviors. No obvious excitonic peaks were observed when the annealing temperature increases from 70 to 110 °C for $(2TIm)_2SnI_4$, and from 70 to 130 °C for $(2TBIm)_2SnI_4$, indicating that the perovskite structure is not formed at low temperature. As the temperature further increases, a small excitonic peak at 560 nm for $(2TIm)_2SnI_4$ and 650 nm for $(2TBIm)_2SnI_4$ present, repectively, which suggests the 2D perovskite structure starts to form. The 2D structures are further confirmed with T-XRD, as a weak peak at 4.7° for $(2TIm)_2SnI_4$ and 4.2° for $(2TBIm)_2SnI_4$ shows up as the annealing temperature increases from 70 °C to 150 °C (**Figure S2**). However,

the $(2TFA)_2SnI_4$ film shows different T-UV behavior with $(2TIm)_2SnI_4$ and $(2TBIm)_2SnI_4$. When the annealing temperature increases from 70 °C to 150 °C, the absorption spectra of $(2TFA)_2SnI_4$ film does not show the appearance of excitonic peak of 2D perovskite. However, a weak peak at 5.0° is observed in the T-XRD of $(2TFA)_2SnI_4$ film, indicating the potential of forming weakly-crystallized 2D structure.

The UV spectra of the Sn- and Pb-perovskites are different from the corresponding UV spectra of ligands, which indicate that the ligands of 2TFAI, 2TImI and 2TBImI reacted with PbI_2 or SnI_2 to form low-dimensional perovskites (**Figure S3**). In addition, the XRD peaks of ligands shift to lower angles when they react with PbI_2, which also suggest the insertion of $[PbI_6]^{4-}$ octahedral between the ligands and formation of low-dimensional perovskite (**Figure S3**). These results suggest that the crystallization behaviors of the OSiPs thin films can be greatly influenced by the anchoring groups and the annealing temperature. Regardless of the metal composition in the inorganic framework, Im- or BIm-based ligands always exhibit similar thin film formation process, due to the similarity in anchoring groups. As increasing the annealing temperature, the conversion presents between different phases formed with imidazole ligand and its derivatives, which indicates that 1D is the stable phase in Pb-based perovskite, while 2D is the stable phase in Sn-based perovskites. In contrast, the FA-based ligand possesses considerable differences in molecular structure comparing with imidazole-based ligands, which causes different crystal formation process, and the possibility of forming weakly crystalline 2D phase.

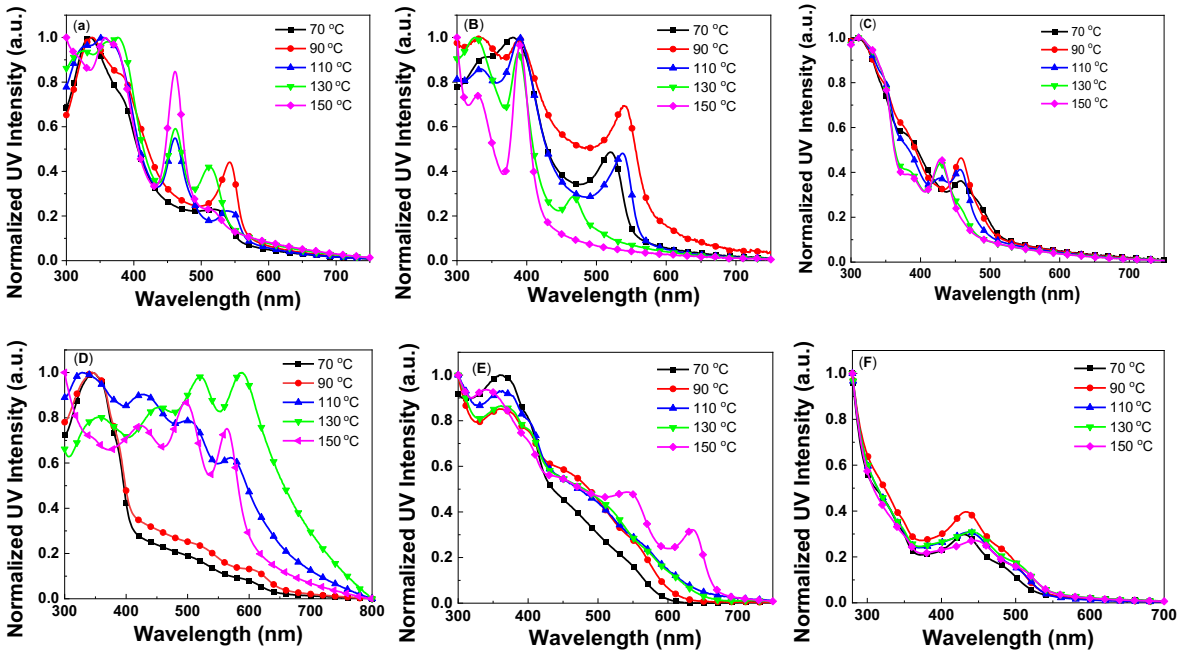

Figure 1. Absorption spectra of films of $(2TIm)_2PbI_4$ (A), $(2TBIm)_2PbI_4$ (B), $(2TFA)_2PbI_4$ (C), $(2TIm)_2SnI_4$ (D), $(2TBIm)_2SnI_4$ (E) and $(2TFA)_2SnI_4$ (F) annealed at different temperatures for 10 min.

2.3. Crystal Structure

To accurately determine the subtleties of the formed structures, single crystal analysis is required. In order to obtain the single crystals of low-dimensional phases, precursor solutions in different solvent with a stoichiometry of A_2BI_4 were prepared (details of the methods can be found in the supporting information, **Table S1**).

Unfortunately, we were unable to obtain single-crystals of the 2D layered perovskite phase (phase 2) with precursor solution of $(2TIm)_2PbI_4$, due to the strong tendency of forming single-crystals of phase 3 (1D), regardless of various precursor stoichiometry. For the synthesis of single-crystals of phase 3, different solvents, including gamma-butyrolactone (GBL), dimethylformamide (DMF) and dimethyl sulfoxide (DMSO), were used in the cooling-down crystal growth method. The empirical formulas of these crystals are $(2TIm)PbI_3 \cdot (GBL)$, $(2TIm)PbI_3 \cdot (DMF)$ and $(2TIm)PbI_3 \cdot (DMSO)$. The inorganic frameworks consist of face-sharing $[PbI_6]^{4-}$ octahedra extend to one dimension, forming 1D structure (**Figure 2**, **Figure S4-S6** and **Table S6-S8**). These 1D perovskite single-crystals possess an inorganic framework of a lower dimensionality than that of the 2D perovskite, which corresponds with excitonic peak of higher energy (phase 3) than that of the 2D perovskite in absorption spectrum. The single crystal synthesized with precursor solution of $(2TBIm)_2PbI_4$ exhibits the same crystalline behavior as $(2TIm)_2PbI_4$. The 1D single crystals including $(2TBIm)PbI_3$, $(2TBIm)_2PbI_3 \cdot (GBL)$ and $(2TBIm)PbI_3 \cdot (DMAC))$ (dimethylacetamide, DMAC), are obtained using different organic solvents (**Figure 2**, **Figure S7-S9** and **Table S9-S11**). These 1D structures match with the 1D phase obtained with 2TImI and 2TBImI ligands at high temperature. While BImI and ImI have been showed as small molecules that can be inserted between inorganic layers to form 1D or 2D perovskites, single crystals were rarely reported to reveal the detailed structures.[21a, c] Here we showed that when BIm and Im are used as anchoring group in a conjugated ligand, the synthesized single crystals adopt a 1D face-sharing structure.

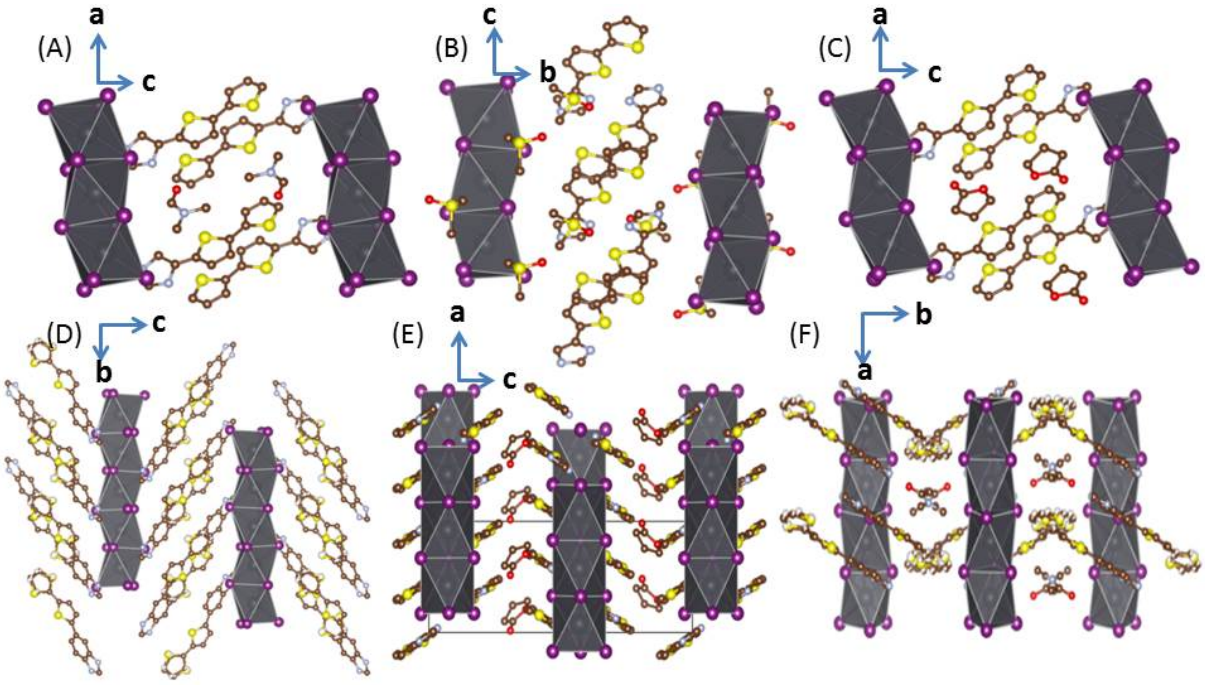

Figure 2. Crystal structure of (2TIm)PbI_3·(DMF), viewed along the b axis (A); (2TIm)PbI_3·(DMSO), viewed along the a axis (B); (2TIm)PbI_3·(GBL), viewed along the b axis (C); (2TBIm)PbI_3, viewed along the a axis (D); (2TBIm)PbI_3·(GBL), viewed along the b axis (E); (2TBIm)PbI_3·(DMAC), viewed along the c axis (F).

Despite of the 2D perovskite properties obtained through T-UV and T-XRD, 2TFAI-based single crystal wasn't able to show the 2D Ruddlesden−Popper (RP) structure. As shown in **Figure 3**, the hypothesized perovskite structure with a formula of $(2TFA)_2PbI_4$ did not form, although the mono-functional organic cation is suitable for being incorporated in perovskite lattice and the precursor solutions are prepared with a stoichiometry of $(2TFA)_2PbI_4$. Instead, $(2TFA)_4Pb_3I_{10}$ crystallizes into the monoclinic space group *Pc*, and the asymmetric unit consists of four organic molecules and one Pb_3I_{10} trimeric unit. The layered crystal structure of $(2TFA)_4Pb_3I_{10}$ is built up from inorganic sheets sandwiched by organic layers (**Figure 3** and **Figure S10**). In the structure of $(2TFA)_4Pb_3I_{10}$, the organic molecules adopt a head to tail arrangement, which can be speculated as existing in solution before the crystallization procession, on account of the π-π interactions and the existence of a dipolar moment caused by the asymmetry of the molecule. The organic layer appears corrugated arrangement with the ammonium functional groups inserting into the voids defined by the inorganic framework. The bithiophene tails of the four independent organic cations are all adopting an anti-conformation. As a consequence of the head to tail arrangement of the molecules, a decrease in the cationic charge density at the interface occurs, leading a condensation of lead octahedra, which means the formation of a new $Pb_3I_{10}^{4-}$ bidimensional iodoplumbate framework. The Pb_3I_{10} trimeric unit in $(2TFA)_4Pb_3I_{10}$ can be described as the non-centrosymmetrical units of

three face-sharing octahedra linked together by iodized vertexes, and two iodine atoms of the trimeric unit linked to only one lead atom (**Figure 3A**). The Pb(1) and Pb(3) octahedra consist of Pb-I bonds with two different bond distances, including three Pb-I_o bonds (mean value of 3.190 Å for Pb(1) and 3.184 Å for Pb(3)) and three Pb-I_i bonds (mean value of 3.249 Å for Pb(1) and 3.251 Å for Pb(3)), in which I_o and I_i represent the outer and the inner iodide atoms of the trimeric unit, respectively (**Figure 3B**, **Table S3**). The six Pb-I bonds of the central octahedron show almost the same distance, ranging from 3.210 to 3.245 Å (**Table S3**). The I-Pb-I bond angles of lead octahedron are in the range of 84.6-96.2° (adjacent iodide) and 169.4-179.9° (opposite iodide). The Pb-I-Pb bond angles between the octahedra range from 73.2° to 75.2°. Using 2TFAI as spacers results in a "Step-Like" (SL) structure, instead of the expected RP structure homologous members. The SL structures involve both corner-sharing and face-sharing $[PbI_6]^{4-}$ octahedra (**Figure 3C**). The resulted trimeric units are linked together to form a SL structure with a dihedral angle of 96.2°, between the mean planes of two consecutive trimmers along b axis. The view of a-b plane in **Figure 3A** and **Figure S10** gives a side view of the SL chains, which extend infinitely along the a axis. The 1D chain in the SL structure is connected by one iodide atom between two trimeric units.

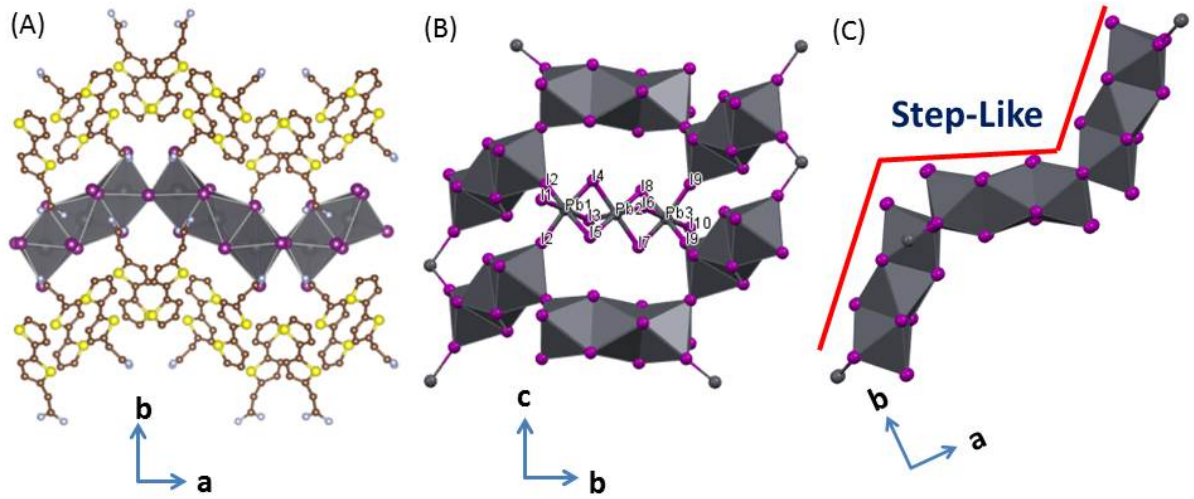

Figure 3. (A) Layered crystal structure of $(2TFA)_4Pb_3I_{10}$, viewed along the c axis; (B) one inorganic sheet, viewed along the a axis; (C) 1D chain of the inorganic sheet.

The Sn-based single crystals with 2TFAI show the similar SL structure as the Pb-based crystal. The $(2TFA)_3Sn_2I_7$ crystals are in the triclinic space group $P\bar{1}$, and the asymmetric unit contains both face- and corner-sharing motifs and three organic cations (**Figure 4** and **Figure S11**). The bithiophene tails of the organic cations are adopting an anti-conformation. Notably, this single crystal adopts a new crystal structure with a composition of $(2TFA)_3Sn_2I_7$, which is different from the Pb-based crystal structure. The Sn-based structure consists of inorganic sheets that are separated by two layers of 2TFAI organic ligands. The inorganic sheets

combine corner- and face-sharing $[SnI_6]^{4-}$ octahedra. The face-sharing structure induces the formation of trimers, where the middle SnI_6-octahedron shares both faces with its neighboring octahedrons. **Figure 4C** shows that the inorganic layers are SL structures due to the stiffness of the face-sharing Sn_3I_{10}-trimer and softness of the corner-sharing SnI_6-monomer. The face-sharing Sn_3I_{10}-trimers are linked to SnI_6-monomer by corner sharing. Moreover, the Sn_3I_{10}-trimers and SnI_6-monomers are arranged alternately. The central octahedron of the trimer contains three different Sn-I bonds with almost the same bond distance, ranging from 3.1685 to 3.1860 Å (**Table S4**). The outer $[SnI_6]^{4-}$ octahedron of the face-sharing Sn_3I_{10}-trimer show two kinds of bonds: one is Sn-I_o with a mean distance of 3.1263 Å; the other is Sn-I_i with a longer mean distance of 3.2374 Å (**Figure 4B**, **Table S4**). The I-Sn-I bond angles of $[SnI_6]^{4-}$ octahedra in the trimers are in the range of 80.68-96.16° (adjacent iodide) and 171.48-174.96° (opposite iodide). The Sn-I-Sn bond angles of the $[SnI_6]^{4-}$ octahedra in the trimers range from 73.50° to 76.92°. The Sn-I bonds and I-Sn-I bond angles of the SnI_6-monomer are in ranges of 3.1457-3.1581 Å and 87.29-94.46°, respectively. The Sn-I-Sn bond angles between the trimer and monomer are 164.93° and 168.47°, respectively. These SL structure formed with 2TFA-based single crystals suggest that even though $FAPbI_3$ is the most promising materials as solar cells and optoelectronic devices, the instable nature of $FAPbI_3$ at room temperature, caused by the large ionic radius of FA^+, is exaggerated when it forms into low-dimensional crystal structures.[23] The distortion of $[PbI_6]^{4-}$ or $[SnI_6]^{4-}$ octahedron inhibits the formation of a normal 1D or 2D corner-sharing perovskite phase.

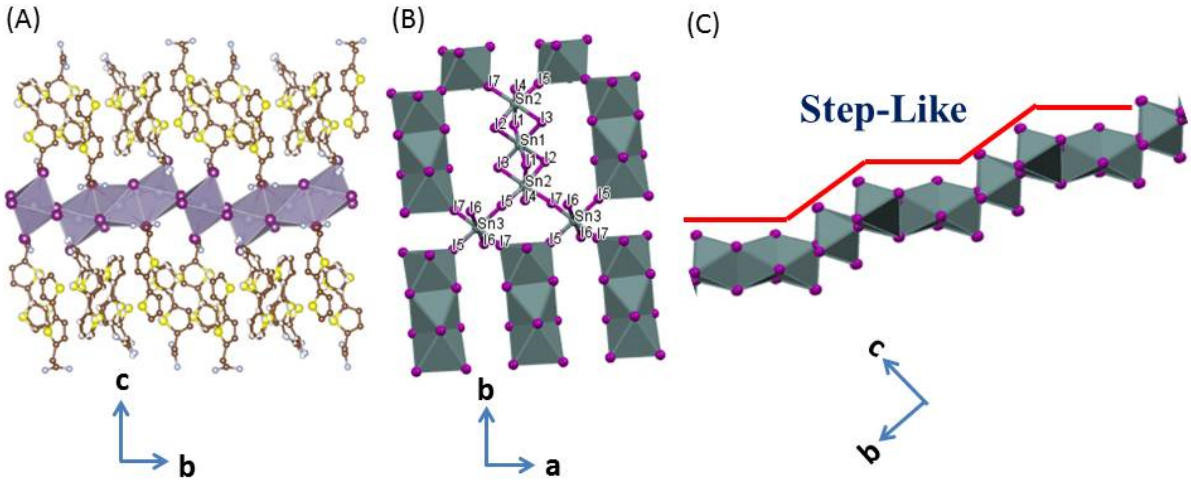

Figure 4. (A) Layered crystal structure of $(2TFA)_3Sn_2I_7$, viewed along the a axis; (B) one inorganic sheet, viewed along the c axis; (C) 1D chain of the inorganic sheet.

Unlike the Sn-based 2TFAI structure, the Sn-based 2TBImI crystal is able to form into 2D RP perovskite structure, evidenced by the single crystal analysis. The crystal structure of $(2TBIm)_2SnI_4 \cdot (DCB)$ is in the space group orthorhombic, $P2_12_12_1$ with the lattice parameters

of a = 6.1142(17) Å, b = 12.365(3) Å, c = 55.809(19) Å. The inorganic perovskite sheets are formed by corner-sharing $[SnI_6]^{4-}$ octahedron units and separated by two layers of head to tail organic ligands (**Figure 5** and **Figure S12**). Notably, *o*-dichlorobenzene (DCB) as the solvent molecules, are intercalated between the two 2TBImI ligands within the same layer. Bond distances and angles of the perovskite sheets are listed in **Table S5**, where the Sn-I bond distances range from 3.008 to 3.240 Å and the I-Sn-I angles are in the range of 86.17-97.19° (adjacent iodide) and 166.50-178.40° (opposite iodide). As can be seen, the neighboring octahedrons are connected almost in a line with the Sn-I-Sn angels of 178.40 and 179.36°. Unfortunately, Sn-base single crystal with ligand of 2TImI wasn't able to be obtained despite many attempts.

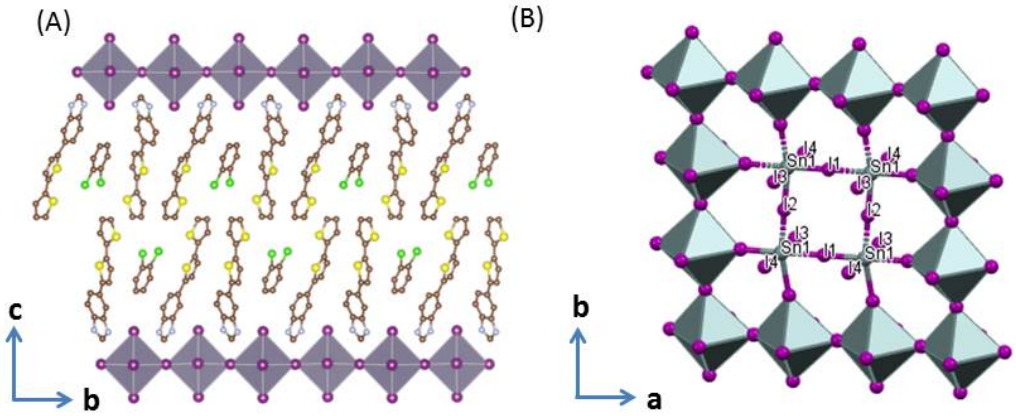

Figure 5. (A) Layered crystal structure of $(2BIm)_2SnI_4 \cdot$(DCB), viewed along the a axis; (B) one inorganic sheet, viewed along the c axis.

Current studies are still limited by the single crystal synthesis to fully understand the different phases we obtained during the film formation and degradation studies. However, the tendency of forming 1D or 2D single crystal structures with 2TImI and 2TBImI indicates the promising potential of applying these structures in optoelectronic devices, despite their bulky head groups. While the octahedron distortion caused by 2TFAI ligand suggests that more effort is required to achieve low-dimensional perovskite phase, this is out of the scope of this report.

2.4 Device Fabrication

The formation of low-dimensional perovskite on the surface of 3D perovskite has been proved as an efficient passivation method to improve the device performance in solar cell field. With the advanced understanding of the interactions between these 2T ligands and the $[PbI_6]^{4-}$ octahedra, we are expecting them to also coordinate with the $[PbI_6]^{4-}$ octahedra in 3D perovskite lattice. Therefore, 2TFAI, 2TImI and 2TBImI are employed in 3D perovskite solar cell devices to investigate the effect of these ligands as passivation ligands on the device

performance. These ligands are applied through post-treatment method. In short, the solution containing passivation ligands was spin-coated on to as-fabricated perovskite thin films, followed by subsequent annealing at 100 °C for 2 min. Chlorobenzene containing 5% (v/v) iso-proponal is used as solvent for passivation ligands, and the brief annealing process is used to dry the solvent. Low concentration of the passivation ligands is adopted to avoid introducing thick low-dimensional perovskite on perovskite surface which may have adverse effect on charge transfer across the interface. Therefore, no visible low-dimensional peaks can be observed in XRD spectra after passivation (**Figure S13**). However, through dipping the perovskite films into the ligand solution and increasing the concentration of ligand solution, the low-angle peaks in XRD spectra become more obvious, which clearly indicate the formation of low-dimensional perovskite after passivation with new ligands (**Figure S14**). The photoluminescence intensities of the 2TImI and 2TBImI passivated perovskite are increased, which suggests the decreased defect density, and decreased non-radiative recombination at perovskite surface (**Figure S15**).

Next, we fabricated the perovskite solar cells with the architecture of ITO/SnO_2/$FAPbI_3$/ligands/Spiro-OMeTAD/Au (**Figure 6A**). The current density-voltage (*J-V*) curves of the corresponding devices are shown in **Figure 6B**. Comparing with the non-treated device, the average V_{OC} increases by 61mV and 74mV for 2TImI and 2TBImI treated devices, respectively. However, devices passivated with 2TFAI didn't show obvious improvement in performance. The statistic results are shown in **Figure S16**. We conducted space-charge limited current (SCLC) measurements on hole-only devices to compare the defect density resulted from different passivation (**Figure S17**). The trap-filling voltage (V_{TFL}) revealed that 2TFAI introduce more defects on to the perovskite surface, while both 2TImI and 2TBImI suppress the surface defects. This finding is corresponded with the single crystal structures we achieved with 2TImI, 2TBImI and 2TFAI. The 1D single crystals of 2TImI and 2TBImI suggest they have better adhesion with 3D perovskite surface, thus can passivate the defects on perovskite surface. Particularly, 2TBImI can form into a pure phase when annealed at 100 ^{o}C, while 2TImI tends to form mixed phases (**Figure S18 and Figure S19**). The SL crystal structure formed between 2TFAI and $[PbI_6]^{4-}$ octahedra might distort the surface structure of 3D perovskite, and unable to coordinate well with the 3D perovskite lattice. Therefore, no improvement in V_{OC} is observed in 2TFAI-passivated devices. Due to the small amount of ligands that is applied on perovskite surface and the weak crystallinity of this low-dimensional crystal, no significant detrimental effect can be observed neither. Overall, the champion efficiency increases from 19.59% for the control device, to 21.13% for the 2TBImI

passivated device, with a V_{OC} of 1.12 V, and the full parameters are listed in **Table S15**. The *J-V* curves of both reverse and forward scans for control device and 2TBImI-passivated device are shown in **Figure 6C**. The passivated device exhibits smaller hysteresis, due to decreased trap density at interface and suppressed ion migration. The current density is confirmed with EQE spectra (**Figure 6D**).

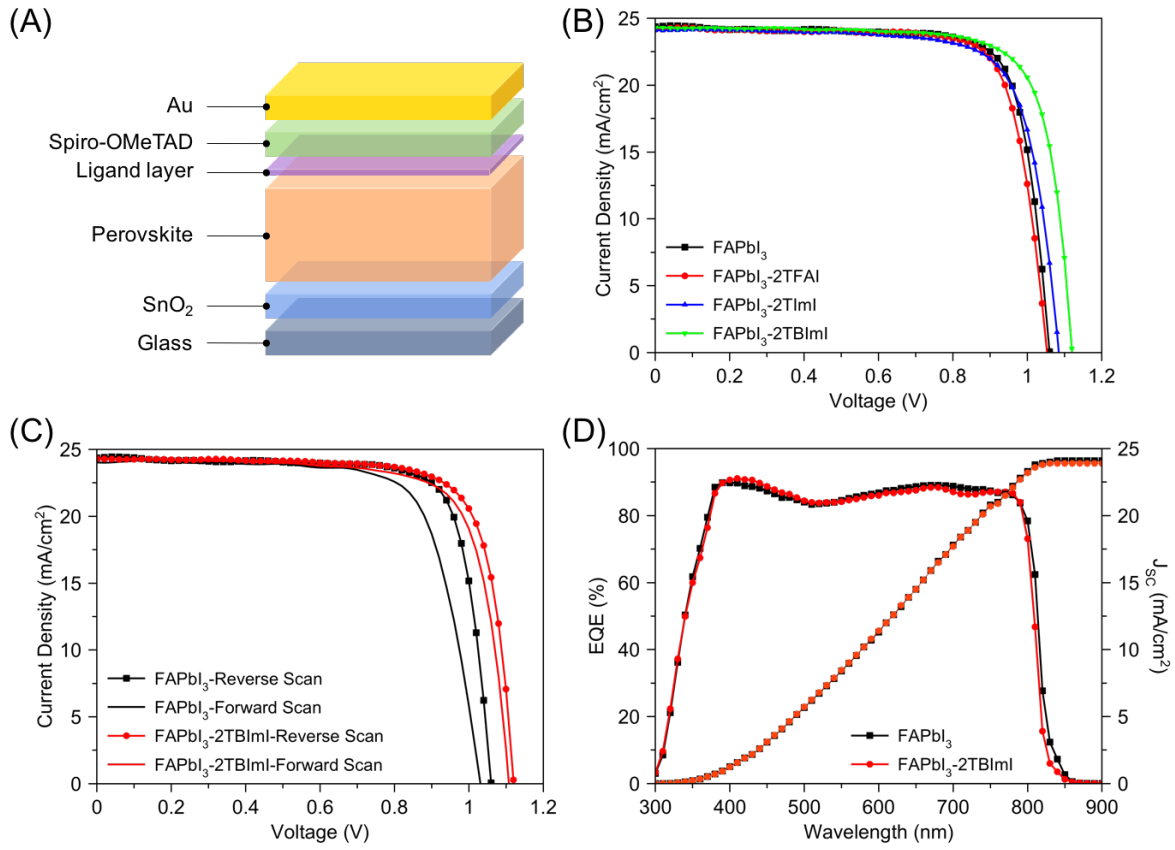

Figure 6. (A) Scheme of perovskite solar cell structure with ligand layer inserted between hole transporting layer and perovskite layer. (B) *J-V* curves of devices with different passivation layers and in comparison with the control device without passivation layer. (C) Champion *J-V* curves of control device and device passivated with 2TBImI, in both reverse scan and forward scan. (D) EQE spectra of control device and device passivated with 2TBImI and the integrated photocurrent density, integrated over the AM1.5 solar spectrum.

3. Conclusion

In summary, we have designed and synthesized a series of functionalized-bithiophene organic ligands with FA, Im and BIm terminal groups, which can greatly influence the crystal structure of low-dimensional perovskites. A series of novel low dimensional Pb- and Sn-based OSiPs have been obtained, and analyzed through single crystal studies. Ligands with Im and BIm terminal groups are able to form 1D or 2D perovskites successfully, while the ligand with FA terminal group will cause distortion of the perovskite octahedron and form "Step-

Like" structures. The importance of the terminal groups in forming low-dimensional perovskites is directly revealed on the solar cell device, which is passivated with these ligands on 3D perovskite surface. Only devices passivated with 2TImI and 2TBImI exhibit improved performance. This improvement in device performance is directly correlated with the low-dimensional crystal structure achieved with these ligands. This work suggests novel anchoring groups are playing a key role in determining crystal structures and properties of OSiPs. Further studies on the electronic and optical properties of these conjugated ligands with different terminal groups will provide more potential applications of them.

4. Experimental Section

4.1. Chemicals and Reagents

Organic solvents, including anhydrous dimethylformide (DMF), dimethyl sulfoxide (DMSO), dimethylacetamide (DMAC), 1,2-dichlorobenzenechlorobenzene (DCB), and γ-butyrolactone (GBL) and solid chemicals, including lead iodide (PbI_2) and tin iodide (SnI_2) were purchased commercially (Sigma Aldrich). All above chemicals were used as received. The ammonium salt ligands, including 2-(5-(thiophen-2-yl)thiophen-2-yl)acetamidinium iodide (2TFAI), 4-(5-(thiophen-2-yl)thiophen-2-yl)-1H-imidazolium iodide (2TImI) and 5-(5-(thiophen-2-yl)thiophen-2-yl)-1H-benzo[d]imidazolium iodide (2TBImI) were synthesized in our lab detailed in Method in the Supporting Information.

4.2. Single crystal growth and characterization

Single crystal growths were conducted by vapor diffusion or cooling down methods with stoichiometric amounts of organic cations and PbI_2 or SnI_2, listed below in **Table S1**. Single crystals were then analyzed using a Bruker Quest diffractometer with a κ geometry, an I-μ-S microsource X-ray tube (Cu K_α radiation, λ = 1.54178 Å), laterally graded multilayer (Goebel) mirror for monochromatization, and a Photon2 CMOS area detector. The instrument is equipped with Oxford Cryosystems low temperature device. The examination and data collection were performed at 150 K. Data were collected, reflections were indexed and processed, and the files were scaled and corrected for absorption using APEX3. The space group was assigned and the structure was solved by direct methods using XPREP within the SHELXTL suite of programs[24] and refined by full matrix least squares against F^2 with all reflections using Shelxl2018 using the graphical interface Shelxle.[25]

Complete crystallographic data, in CIF format, have been deposited with the Cambridge Crystallographic Data Centre. CCDC 2111441, 2111442, 2111443, 2111445, 2111446, 2111448, 2111449, 2111450 and 2111453 contain the supplementary crystallographic data for

this paper. It can be obtained free of charge from The Cambridge Crystallographic Data Centre via www.ccdc.cam.ac.uk/data_request/cif.

4.3. Low-dimensional perovskite thin film preparation

Bare quartz slides were used as the substrates for spin coating the perovskite thin films. The substrates were cleaned by ultrasonication in water, acetone, isopropanol, and isopropanol again for 5 min in a sequential manner; then, they were dried using a nitrogen gun. The substrates were treated with UV-ozone for 10 min then transferred into a glove box for further use. As synthesized 2TImI (36.1 mg, 100 μmol) or 2TBImI (41.1 mg, 100 μmol) or 2TFAI (35.1 mg, 100 μmol) and SnI_2 (18.6 mg, 50 μmol) or PbI_2 (23.0 mg, 50 μmol) were dissolved in 1 mL of anhydrous DMF at 70 ^oC under constant stirring. The precursor solutions were allowed to cool to room temperature for spin coating. Films for optical measurements and XRD analysis were deposited on quartz substrates using spin coating in a glovebox with nitrogen atmosphere at 4000 rpm for 60 s, followed by thermal annealing at different temperatures (70-150 ^oC) on a hot plate for 10 min in nitrogen.

4.4. Characterization

NMR spectra were acquired at room temperature using a Bruker AV 400-MHz spectrometer with $CDCl_3$ or *d*-DMSO as the solvent and tetramethylsilane (TMS) as an internal standard. Chemical shifts of ^1H NMR signals were reported as values (ppm) relative to the TMS standard. Samples were analyzed on an LTQ Orbitrap mass spectrometer (ThermoFisher Scientific, Bremen, Germany) using a high resolution scan setting of 60000. After tuning and calibrating the instrument in positive mode with a Thermo LTQ positive ion calibration solution the samples were analyzed in ESI (Electrospray) and Atmospheric Pressure Chemical Ionization (APCI) modes. Thin film out-of-plane XRD data were acquired using a Rigaku Smart Lab using a Cu K_α source (λ= 1.54056 Å) in Bragg Brentano mode. Thin film samples were spin-coated on highly n-doped silicon wafers covered with a 300 nm thick thermally grown SiO_2 dielectric layer. Thin film absorption spectra were recorded on an Agilent UV-Vis-NIR Cary-5000 spectrometer in transmission mode.

4.5 Device Fabrication

The ITO substrate was cleaned with water, acetone and isoproponal sequentially, and then treated with UVO-zone for 30 min just before device fabrication. The SnO_2 nanoparticle suspension (1.67%) was spin coated onto ITO substrate at 3,000 rpm for 30 s, followed by annealing at 150 °C for 30 min. KOH (10mM) solution was spin coated on SnO_2 layer as interface modification. The perovskite solution was prepared by dissolving 1.53 M PbI_2, 1.4 M FAI, 0.5 M MACl and 0.0122 M $MAPbBr_3$ in DMSO:DMF=1:8. The as-fabricated SnO_2

was treated with UVO-zone for 20 min, and transferred into glove box for the following process. The perovskite layer was deposited by spin coating 30 μL of precursor solution onto SnO_2 at a speed of 1000 rpm for 10 s, and 5000 rpm for 30 s. 600uL diethyl ether was dropped onto the perovskite layer at 20 s before the end of the spin. The as-casted perovskite film was annealed at 100 °C for 60 min. The ligand solutions (contains 0.5 mg/mL ligand), prepared in chlorobenzene and isoproponal mixture, was spin coated onto perovskite surface at 4,000 rpm followed by annealing at 100 °C for 2 min. We observed no differences in device performance with or without annealing, thus annealing is only used to evaporate solvent. The spiro-OMeTAD solution (51.5 mg/mL spiro-OMeTAD in 600uL CB, 20.28 μL tBP and 11.73 μL of 520 mg/mL Li-TFSI) was spin coated onto perovskite film as the hole transporting layer. The device was finished with evaporation of 90 nm Au as top electrode.

4.6 Device and film characterizaion

The steady-state photoluminescence spectra were collected with a SpectraPro HRS-300. J-V characteristics were measured using simulated AM1.5G irradiation (100 mW/cm^2), produced by a solar simulator from Enlitech (SS-F5-3A). A Keithley 2450 SourceMeter was used for the *J-V* curve measurements. The active area is 0.048 cm^2, defined by the Au electrode deposition mask. The EQE measurements were performed on home-built equipment with a preamplifier and a lock-in amplifier at chopper frequency of 161 Hz. The measurements were calibrated with a reference UV-enhanced Si diode (818-UV-L).

[CCDC 2111441, 2111442, 2111443, 2111445, 2111446, 2111448, 2111449, 2111450 and 2111453 contain the supplementary crystallographic data for this paper. These data can be obtained free of charge from The Cambridge Crystallographic Data Centre via www.ccdc.cam.ac.uk/data_request/cif.]

Supporting Information

Supporting Information is available from the Wiley Online Library or from the author.

Acknowledgements

Materials synthesis was supported by the US Office of Naval Research (no. N00014-19-1-2296). Device fabrication was supported by National Science Foundation (no. 2131608-ECCS). Aihui Liang was supported by the National Natural Science Foundation of China (No. 51763013) and Overseas Promotion Program for Young Academic Leaders of Jiangxi Normal University.)

Received: ((will be filled in by the editorial staff))
Revised: ((will be filled in by the editorial staff))
Published online: ((will be filled in by the editorial staff))

References

[1] a) M. Jeong, I. W. Choi, E. M. Go, Y. Cho, M. Kim, B. Lee, S. Jeong, Y. Jo, H. W. Choi, J. Lee, J.-H. Bae, S. K. Kwak, D. S. Kim, C. Yang, *Science* **2020**, *369*, 1615; b) Q. A. Akkerman, M. Gandini, F. Di Stasio, P. Rastogi, F. Palazon, G. Bertoni, J. M. Ball, M. Prato, A. Petrozza, L. Manna, *Nat. Energy* **2016**, *2*, 16194; c) F. Sahli, J. Werner, B. A. Kamino, M. Bräuninger, R. Monnard, B. Paviet-Salomon, L. Barraud, L. Ding, J. J. Diaz Leon, D. Sacchetto, G. Cattaneo, M. Despeisse, M. Boccard, S. Nicolay, Q. Jeangros, B. Niesen, C. Ballif, *Nat. Mater.* **2018**, *17*, 820; d) F. Hao, C. C. Stoumpos, D. H. Cao, R. P. H. Chang, M. G. Kanatzidis, *Nat. Photonics* **2014**, *8*, 489.

[2] a) L. Dou, Y. Yang, J. You, Z. Hong, W.-H. Chang, G. Li, Y. Yang, *Nat, Commun.* **2014**, *5*, 5404; b) R. Dong, Y. Fang, J. Chae, J. Dai, Z. Xiao, Q. Dong, Y. Yuan, A. Centrone, X. C. Zeng, J. Huang, *Adv. Mater.* **2015**, *27*, 1912; c) C. Li, Y. Ma, Y. Xiao, L. Shen, L. Ding, *InfoMat* **2020**, *2*, 1247; d) H.-P. Wang, S. Li, X. Liu, Z. Shi, X. Fang, J.-H. He, *Adv. Mater.* **2021**, *33*, 2003309.

[3] a) Y. Liang, F. Li, R. Zheng, *Adv. Electron. Mater.* **2020**, *6*, 2000137; b) H. Zhu, A. Liu, K. I. Shim, J. Hong, J. W. Han, Y.-Y. Noh, *Adv. Mater.* **2020**, *32*, 2002717; c) T. Matsushima, S. Hwang, A. S. D. Sandanayaka, C. Qin, S. Terakawa, T. Fujihara, M. Yahiro, C. Adachi, *Adv. Mater.* **2016**, *28*, 10275; d) Y. Gao, Z. Wei, P. Yoo, E. Shi, M. Zeller, C. Zhu, P. Liao, L. Dou, *J. Am. Chem. Soc.* **2019**, *141*, 15577; e) I.-H. Park, K. C. Kwon, Z. Zhu, X. Wu, R. Li, Q.-H. Xu, K. P. Loh, *J. Am. Chem. Soc.* **2020**, *142*, 18592.

[4] a) Z.-K. Tan, R. S. Moghaddam, M. L. Lai, P. Docampo, R. Higler, F. Deschler, M. Price, A. Sadhanala, L. M. Pazos, D. Credgington, F. Hanusch, T. Bein, H. J. Snaith, R. H. Friend, *Nat. Nanotechnol.* **2014**, *9*, 687; b) A. Liang, K. Wang, Y. Gao, B. P. Finkenauer, C. Zhu, L. Jin, L. Huang, L. Dou, *Angew. Chem. Int. Ed.* **2021**, *60*, 8337; c) K. Wang, L. Jin, Y. Gao, A. Liang, B. P. Finkenauer, W. Zhao, Z. Wei, C. Zhu, T.-F. Guo, L. Huang, L. Dou, *ACS Nano* **2021**, *15*, 6316; d) H. Wang, X. Gong, D. Zhao, Y.-B. Zhao, S. Wang, J. Zhang, L. Kong, B. Wei, R. Quintero-Bermudez, O. Voznyy, Y. Shang, Z. Ning, Y. Yan, E. H. Sargent, X. Yang, *Joule* **2020**, *4*, 1977; e) Y. Cao, N. Wang, H. Tian, J. Guo, Y. Wei, H. Chen, Y. Miao, W. Zou, K. Pan, Y. He, H. Cao, Y. Ke, M. Xu, Y. Wang, M. Yang, K. Du, Z. Fu, D. Kong, D. Dai, Y. Jin, G. Li, H. Li, Q. Peng, J. Wang, W. Huang, *Nature* **2018**, *562*, 249.

[5] a) Q. Chen, H. Zhou, Z. Hong, S. Luo, H.-S. Duan, H.-H. Wang, Y. Liu, G. Li, Y. Yang, *J. Am. Chem. Soc.* **2014**, *136*, 622; b) Q. Wang, Y. Shao, Q. Dong, Z. Xiao, Y. Yuan, J. Huang, *Energy Environ. Sci.* **2014**, *7*, 2359; c) Y. Gao, E. Shi, S. Deng, S. B. Shiring, J. M. Snaider, C. Liang, B. Yuan, R. Song, S. M. Janke, A. Liebman-Peláez, P. Yoo, M. Zeller, B. W. Boudouris, P. Liao, C. Zhu, V. Blum, Y. Yu, B. M. Savoie, L. Huang, L. Dou, *Nat. Chem.* **2019**, *11*, 1151; d) M. Liu, M. B. Johnston, H. J. Snaith, *Nature* **2013**, *501*, 395.

[6] A. Mei, X. Li, L. Liu, Z. Ku, T. Liu, Y. Rong, M. Xu, M. Hu, J. Chen, Y. Yang, M. Grätzel, H. Han, *Science* **2014**, *345*, 295.

[7] a) S. D. Stranks, G. E. Eperon, G. Grancini, C. Menelaou, M. J. P. Alcocer, T. Leijtens, L. M. Herz, A. Petrozza, H. J. Snaith, *Science* **2013**, *342*, 341; b) G. Xing, N. Mathews, S. Sun, S. S. Lim, Y. M. Lam, M. Grätzel, S. Mhaisalkar, T. C. Sum, *Science* **2013**, *342*, 344.

[8] a) S. H. Cho, J. Byeon, K. Jeong, J. Hwang, H. Lee, J. Jang, J. Lee, T. Kim, K. Kim, M. Choi, Y. S. Lee, *Adv. Energy Mater.* **2021**, *11*, 2100555; b) E. Shi, Y. Gao, B. P. Finkenauer, Akriti, A. H. Coffey, L. Dou, *Chem. Soc. Rev.* **2018**, *47*, 6046.

[9] a) B. Zhao, Y. Lian, L. Cui, G. Divitini, G. Kusch, E. Ruggeri, F. Auras, W. Li, D. Yang, B. Zhu, R. A. Oliver, J. L. MacManus-Driscoll, S. D. Stranks, D. Di, R. H. Friend, *Nat. Electron.* **2020**, *3*, 704; b) H. Cho, S.-H. Jeong, M.-H. Park, Y.-H. Kim, C. Wolf, C.-L. Lee,

J. H. Heo, A. Sadhanala, N. Myoung, S. Yoo, S. H. Im, R. H. Friend, T.-W. Lee, *Science* **2015**, *350*, 1222.

[10] J. Jeong, M. Kim, J. Seo, H. Lu, P. Ahlawat, A. Mishra, Y. Yang, M. A. Hope, F. T. Eickemeyer, M. Kim, Y. J. Yoon, I. W. Choi, B. P. Darwich, S. J. Choi, Y. Jo, J. H. Lee, B. Walker, S. M. Zakeeruddin, L. Emsley, U. Rothlisberger, A. Hagfeldt, D. S. Kim, M. Grätzel, J. Y. Kim, *Nature* **2021**, *592*, 381.

[11] a) Y. Rong, Y. Hu, A. Mei, H. Tan, M. I. Saidaminov, S. I. Seok, M. D. McGehee, E. H. Sargent, H. Han, *Science* **2018**, *361*, eaat8235; b) T.-S. Su, F. T. Eickemeyer, M. A. Hope, F. Jahanbakhshi, M. Mladenović, J. Li, Z. Zhou, A. Mishra, J.-H. Yum, D. Ren, A. Krishna, O. Ouellette, T.-C. Wei, H. Zhou, H.-H. Huang, M. D. Mensi, K. Sivula, S. M. Zakeeruddin, J. V. Milić, A. Hagfeldt, U. Rothlisberger, L. Emsley, H. Zhang, M. Grätzel, *J. Am. Chem. Soc.* **2020**, *142*, 19980.

[12] N. J. Jeon, J. H. Noh, W. S. Yang, Y. C. Kim, S. Ryu, J. Seo, S. I. Seok, *Nature* **2015**, *517*, 476.

[13] Z. Gu, L. Zuo, T. T. Larsen-Olsen, T. Ye, G. Wu, F. C. Krebs, H. Chen, *J. Mater. Chem. A* **2015**, *3*, 24254.

[14] a) H. Zhu, Y. Ren, L. Pan, O. Ouellette, F. T. Eickemeyer, Y. Wu, X. Li, S. Wang, H. Liu, X. Dong, S. M. Zakeeruddin, Y. Liu, A. Hagfeldt, M. Grätzel, *J. Am. Chem. Soc.* **2021**, *143*, 3231; b) L. Qiu, S. He, L. K. Ono, Y. Qi, *Adv. Energy Mater.* **2020**, *10*, 1902726.

[15] Q. Dong, F. Liu, M. Wong, H. Tam, A. Djurišić, A. Ng, C. Surya, W. K. Chan, A. M. C. Ng, *ChemSusChem* **2016**, *9*, 2518.

[16] K. Wang, J. Y. Park, Akriti, L. Dou, *EcoMat* **2021**, *3*, e12104.

[17] a) W. T. M. Van Gompel, R. Herckens, K. Van Hecke, B. Ruttens, J. D'Haen, L. Lutsen, D. Vanderzande, *ChemNanoMat* **2019**, *5*, 323; b) Y. Takeoka, K. Asai, M. Rikukawa, K. Sanui, *Chem. Commun.* **2001**, 2592; c) M. Era, T. Kobayashi, K. Sakaguchi, E. Tsukamoto, Y. Oishi, *Org. Electron.* **2013**, *14*, 1313; d) K.-z. Du, Q. Tu, X. Zhang, Q. Han, J. Liu, S. Zauscher, D. B. Mitzi, *Inorg. Chem.* **2017**, *56*, 9291.

[18] a) W. A. Dunlap-Shohl, E. T. Barraza, A. Barrette, S. Dovletgeldi, G. Findik, D. J. Dirkes, C. Liu, M. K. Jana, V. Blum, W. You, K. Gundogdu, A. D. Stiff-Roberts, D. B. Mitzi, *Mater. Horiz.* **2019**, *6*, 1707; b) C. Liu, W. Huhn, K.-Z. Du, A. Vazquez-Mayagoitia, D. Dirkes, W. You, Y. Kanai, D. B. Mitzi, V. Blum, *Phys. Rev. Lett.* **2018**, *121*, 146401; c) S. Deng, J. M. Snaider, Y. Gao, E. Shi, L. Jin, R. D. Schaller, L. Dou, L. Huang, *J. Chem. Phys.* **2020**, *152*, 044711.

[19] Y. Gao, L. Dou, *Natl. Sci. Rev.* **2021**, DOI:10.1093/nsr/nwab111.

[20] a) Y. Gao, Z. Wei, S.-N. Hsu, B. W. Boudouris, L. Dou, *Mater. Chem. Front.* **2020**, *4*, 3400; b) A. Liang, Y. Gao, R. Asadpour, Z. Wei, B. P. Finkenauer, L. Jin, J. Yang, K. Wang, K. Chen, P. Liao, C. Zhu, L. Huang, B. W. Boudouris, M. A. Alam, L. Dou, *J. Am. Chem. Soc.* **2021**, *143*, 15215; c) D. B. Mitzi, K. Chondroudis, C. R. Kagan, *Inorg. Chem.* **1999**, *38*, 6246; d) J. V. Passarelli, D. J. Fairfield, N. A. Sather, M. P. Hendricks, H. Sai, C. L. Stern, S. I. Stupp, *J. Am. Chem. Soc.* **2018**, *140*, 7313.

[21] a) E. A. Alharbi, A. Y. Alyamani, D. J. Kubicki, A. R. Uhl, B. J. Walder, A. Q. Alanazi, J. Luo, A. Burgos-Caminal, A. Albadri, H. Albrithen, M. H. Alotaibi, J.-E. Moser, S. M. Zakeeruddin, F. Giordano, L. Emsley, M. Grätzel, *Nat, Commun.* **2019**, *10*, 3008; b) I. Zimmermann, S. Aghazada, M. K. Nazeeruddin, *Angew. Chem. Int. Ed.* **2019**, *58*, 1072; c) Y. Zhan, F. Yang, W. Chen, H. Chen, Y. Shen, Y. Li, Y. Li, *Adv. Mater.* **2021**, DOI: 10.1002/adma.202105170.

[22] W. T. M. Van Gompel, R. Herckens, P.-H. Denis, M. Mertens, M. C. Gélvez-Rueda, K. Van Hecke, B. Ruttens, J. D'Haen, F. C. Grozema, L. Lutsen, D. Vanderzande, *J. Mater. Chem. C* **2020**, *8*, 7181.

[23] Y. An, J. Hidalgo, C. A. R. Perini, A.-F. Castro-Méndez, J. N. Vagott, K. Bairley, S. Wang, X. Li, J.-P. Correa-Baena, *ACS Energy Lett.* **2021**, *6*, 1942.

[24] G. Sheldrick, *Acta Crystallogr. A* **2008**, *64*, 112.
[25] a) G. Sheldrick, *Acta Crystallogr. C* **2015**, *71*, 3; b) C. B. Hübschle, G. M. Sheldrick, B. Dittrich, *J. Appl. Crystallogr.* **2011**, *44*, 1281.

A series of bithiophene-based conjugated ligands with formamidinium, imidazolium and benzimidazolium terminal groups are synthesized to examine the influence of different anchoring groups on the crystal structures, phase formaton, and device performances. Perovskite solar cells passivated by the low dimensional OSiPs containing benzimidazolium cations exhibit enhanced power conversion efficiencies and reduced hysteresis.

A. Liang, K. Ma, Y. Gao, L. Dou*

Tailoring Anchoring Groups in Low-Dimensional Organic Semiconductor-Incorporated Perovskites